Biomaterials Science

PAPER

View Article Online
View Journal

Cite this: DOI: 10.1039/d5bm01877c

Supramolecular RNAi with multifunctional siRNA nanostructures

Michael Shaikhet,†[c] Joshua O'Grady,†[a] Filiz K. Collak,†[a,b] Matthew Reynolds,[c] Anatoli Ianoul,[a,c] William G. Willmore,[a,b,c] Bruce C. McKay[b,c] and David Sabatino *[a,c]

Supramolecular RNA nanostructures have recently emerged as powerful genetic tools in biomedical applications. The modular design of discrete RNA building block monomers for the self-assembly of genetically encoded short interfering RNA (siRNA) nanostructures has led to the precise silencing of oncogene targets in cancer gene therapy applications. In this study, we designed and synthesized V- and Y-shaped branched RNA templates to scaffold the assembly of well-defined 2D- and 3D-shaped siRNA nanostructures targeting the oncogenic mRNA transcripts of Glucose Regulated Proteins (GRP75, 78, 94, 170) in cancer. Structure and stability analyses confirmed the formation of siRNA nano-squares, -cubes and -tubes with distinct supramolecular and biophysical properties. Bioconjugation strategies enabled the incorporation of fluorescein and coumarin fluorescent reporters, providing FRET-based biosensing of the dynamic assembly process of the siRNA nanostructures. In the human adenocarcinoma (A549) cell line, the fluorescently labelled siRNA nanostructures demonstrated cell uptake and intracellular localization for GRP silencing events that led to significant anti-proliferative and toxicity effects, as indicators of anti-cancer activity. This research will highlight the innovation of multifunctional siRNA nanostructures for applications in cancer gene-silencing therapies.

Received 22nd December 2025,
Accepted 18th March 2026

DOI: 10.1039/d5bm01877c

rsc.li/biomaterials-science

Introduction

The rapidly evolving field of RNA nanotechnology has led to the production of functional RNA biomaterials for their advancement in chemical biology, bioengineering and biotechnology, in addition to therapeutic applications.[1–8] The strong tendency for RNA to engage in stable, high fidelity Watson–Crick base-pairing provides structure programmability that scaffolds the self-assembly of higher-ordered supramolecular architectures displaying distinct sizes, shapes and functions.[9,10] Various self-assembly tools have been designed and developed for the formulation of discrete RNA nanostructures. These include modular building blocks (*i.e.*, RNA architectonics) that preorganize (bottom-up) levels of higher-ordered RNA structure organization,[11,12] oligonucleotide templates that enable assembly of complementary RNA (origami) patterned motifs,[13,14] and machine learning tools that predict RNA folding and self-assembly of nanostructures based on sequence information.[15,16] Of particular interest are the assembly strategies that incorporate bio-active RNA sequences to produce genetically encoded supramolecular structures with novel functional properties in biological systems.

Short-interfering RNA (siRNA) nanostructures have been used for silencing single or multiple oncogenic (mRNA) targets *via* the RNA interference (RNAi) pathway for applications in cancer therapy.[17–22] In these studies, DNA and RNA templates have been applied in the co-transcriptional assembly of siRNA nanostructures representing a variety of 2D and 3D shapes. Moreover, functionalization of the siRNA assemblies with modified nucleotides (*e.g.*, 2′-F-dNTPs), lipids for cell delivery, fluorochromes for fluorescence and FRET detection and targeting aptamers has been found to enhance RNA structure and function in cell-based and *in vivo* cancer models.[17–22] The observed safety and efficacy profiles of RNA nanoparticles make them desirable drug candidates for future clinical translational studies.[23] However, these assembly methods are also susceptible to forming multiple undesirable (nano)structures due to the propensity for RNA folding into various stable secondary and tertiary structure motifs and greater tolerance for nucleotide mismatch incorporation during transcriptional enzymatic polymerization, which makes it difficult to build discrete RNA nanostructures.[24] Furthermore, optimization in the batch-scale production of chemically modified RNA nanostructures is needed to improve RNA pharmacological properties for clinical use.[25] Pre-defined RNA building blocks with

[a]*Department of Chemistry, Carleton University, 1125 Colonel By Drive, Ottawa, ONK1S 5B6 8, Canada. E-mail: david.sabatino@carleton.ca*
[b]*Department of Biology, Carleton University, 1125 Colonel By Drive, Ottawa, ONK1S 5B6 8, Canada*
[c]*Institute of Biochemistry, Carleton University, 1125 Colonel By Drive, Ottawa, ONK1S 5B6 8, Canada*
†M. S., J. O. and F. K. C. contributed equally to this work.

chemical modifications can be readily manufactured by automated solid phase oligonucleotide synthesis and combined to form a limitless number of distinct supramolecular architectures with novel functional properties for the translation of siRNA nanostructures in clinical oncology.[26,32]

In our previous research, the incorporation of a synthetic branchpoint nucleotide modification enabled the construction of branched and hyperbranched (dendrimer-type) siRNAs with improved stability and function for anti-cancer applications.[27] The branched siRNAs triggered knockdown of the oncoprotein, glucose regulated protein of 78 kilodaltons (GRP78), which led to greater toxicity in HepG2 liver cancer cells when compared to the control, linear siRNA treatment conditions. Moreover, the synthetic branched RNAs were used as single-stranded templates in combination with complementary RNA sequences to assemble well-defined siRNA nanostructures, which resembled a variety of 2D polygons, such as nano-squares, rectangles, pentagons and hexagons, among others, of distinct sizes and shapes.[28] The siRNA nanostructures displayed enhanced serum stability, which extended their duration of action in silencing the expression of the oncogenic glucose regulated proteins of 75, 78, and 94 kilodaltons (GRP75, 78 and 94), resulting in antiproliferative effects across a panel of cancer cell lines over a prolonged (72 h) treatment period.[28] The synergistic multi-GRP knockdown effect led to potent toxicity in breast (MDA MB-231), cervical (HeLa) and endometrial (AN3CA) cancer cell lines, and to a greater extent with the siRNA nanostructures compared to linear GRP siRNA controls, even when added in combination.[28] Bioconjugation of siRNA nanostructures with fatty acids, metal nanoparticles and fluorescent reporters enhanced cell delivery, detection and treatment efficacy in cancer.[29–31] Therefore, multifunctional siRNA nanostructures represent a promising class of therapeutic modalities in cancer diagnosis and therapy.[32]

In this current work, the incorporation of multiple siRNAs targeting all main GRPs (GRP75, GRP78, GRP94, GRP170) into novel supramolecular 2D and 3D nanostructure assemblies (Fig. 1) was hypothesized to maximize the GRP-silencing and anti-tumour effects in human lung (A549) adenocarcinoma (ATCC® CCL-185™) cells. A solid phase chemical synthesis strategy was used to produce V- and Y-shaped branched RNA templates for the assembly of multiple siRNA units into discrete and defined nanostructure formulations. Bioconjugation enabled chemo- and regiospecific functionalization of siRNA nanostructures with fluorochromes used for the study of their structural, photophysical and biological properties. This research aims to impact cancer intervention strategies using multifunctional siRNA nanostructures.

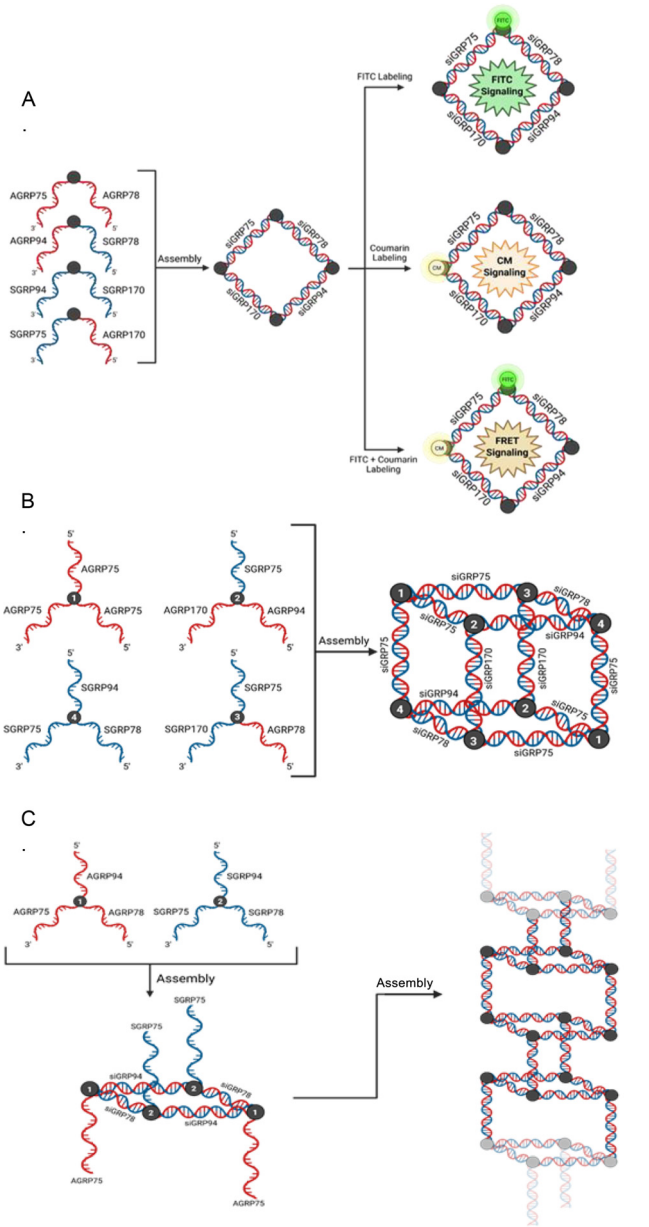

Fig. 1 Formulation of supramolecular siRNA nanostructures. (A) Assembly of the siRNA square from V-shaped RNA templates and fluorochrome (coumarin (CM) and fluorescein isothiocyanate (FITC)) labelling. (B) Assembly of the siRNA cube from Y-shaped RNA templates. (C) Toehold assembly strategy for the siRNA tube from the Y-shaped RNA templates. Created in BioRender. Shaikhet, M. (2025) https://BioRender.com/y6scwfz and https://BioRender.com/lmo6wl6.

Results and discussion

Rational design of RNA templates for supramolecular assembly of siRNA nanostructures

The antisense (A) and sense (S) strand siRNA sequences (SI, Table S1) have been used to effectively and specifically silence oncogenic mRNA transcripts encoding the GRPs (GRP75, 78, 94, and 170) in human cancer cell lines, resulting in potent anti-cancer effects.[28,33] The GRPs function as biomolecular chaperones that serve as main sensors for misfolded proteins in the endoplasmic reticulum (ER) and function as master regulators of cell survival and apoptosis under cell stress conditions as part of the unfolded protein response (UPR) mechanism.[34] The GRPs are over-expressed and translocated to the

surface of many types of human cancer cell lines, where they act as tumour biomarkers and activate signalling pathways linked to cancer initiation, proliferation, metastasis and chemoresistance.[35] GRP knockdown or inhibition has been shown to sensitize cancer cells to treatment and promote tumour cell cycle arrest and apoptosis, resulting in potent anti-cancer effects.[28–33,35] Thus, targeting the GRPs offers a promising approach in the diagnosis and treatment of cancer.[35] In this study, novel 2D and 3D supramolecular RNA assemblies were designed and constructed as well-defined, discrete square, cube, and tube shaped GRP-silencing siRNA nanostructures (Fig. 1).

The complementary GRP silencing siRNA (A : S) sequences[28,33] (Table S1) were directly integrated at the branchpoint positions of the V- and Y-shaped branched RNA templates. They were combined in controlled stoichiometric equivalent ratios and annealed in their antiparallel orientations to generate double-stranded (ds) RNA helical hybrids of equal lengths, 19 base-pairs, which avoided off-target hybridization and self-folding interactions while templating the assembly of discrete supramolecular square, cube, and tube shaped siRNA nanostructures (Fig. 1). To validate GRP mRNA transcript (sense-strand) specificity, each of the antisense strands in the siRNA sequences (SI, Table S1) was evaluated using NCBI BLAST (blastn) against the human RefSeq RNA database (SI, Table S4). In all cases, the GRP sequences maintained the largest query coverage and the lowest *E*-values, corresponding to full-length (A : S) complementarity with no significant matches to unrelated off-target and immunogenic transcripts. The siRNA sequences were also tested computationally for secondary structure formation and self-folding during the hybridization process. All sequences showed weak self-folding capabilities, while hybridization to dsRNA was thermodynamically favoured. Thus, the siRNA sequences were anticipated to form stable RNA hybrids, templating the assembly of discrete supramolecular siRNA nanostructures (Fig. 1).

For example, to build the square shaped siRNA nanostructure (Fig. 1A), four complementary V-shaped RNA templates (GRPA75A78, A94S94, S75A170, and S94S170) were selected to hybridize into antiparallel dsRNA helices that were genetically encoded as siRNAs targeting all GRPs in an enclosed square shaped nanostructure. Moreover, the incorporation of fluorochromes (*e.g.*, coumarin (CM) and fluorescein isothiocyanate (FITC)) at the branchpoint position was rationalized to facilitate structural, photochemical and biological studies.[29,32,36] Similarly, a cube shaped siRNA nanostructure was designed with four distinct Y-shaped RNA templates (A75A75A75, S75S78S94, A170A94S75, and S170A78A75, Fig. 1B), which combine complementary (A : S) sequences to produce multiple GRP-silencing siRNAs (*i.e.*, 6× siGRP75, 2× siGRP78, 2× siGRP94 and 2× siGRP170) in a closed 3D geometry resembling a cubic-shaped nanostructure. The nanotube design employed a stacked toe-hold assembly strategy as an extension of the square-shaped siRNA nanostructure (Fig. 1C). In this approach, repeated monomeric cubic units were hypothesized to assemble into an extended nanotube structure with consistent 3D (length, width and height) measurements across the nanotube. This intricate nanostructure was designed with only two Y-shaped RNA templates (A75A78A94 and S75S78S94), genetically encoding three (GRP75, 78 and 94) siRNAs, but not GRP170 siRNA within the nanotube assembly. The Y-shaped RNA templates were selected to form a square shaped siRNA framework, with complementary (A : S) single-stranded (ss) RNA overhangs (toe-holds) at the branchpoint positions that enable end-to-end joining of the 2D square framework into a modular, stacked assembly of 3D cubic monomers for nanotube elongation. The design of discrete RNA building blocks for the assembly of genetically encoded short interfering RNA (siRNA) nanostructures is important to the study of their structural, photophysical and biological properties.

Solid-phase synthesis of functionalized RNA templates

The chemical synthesis of RNA templates followed the standard automated solid-phase oligonucleotide synthesis cycle involving four major steps: (1) detritylation, to remove the 5′-dimethoxytrityl (DMT) protecting group of a preloaded thymidine linked controlled pore glass (CPG) support and to expose the 5′-hydroxyl (OH) group for subsequent reactions; (2) activation and coupling of the 5′-DMT 2′-*tert*-butyldimethylsilyl (TBDMS) ribonucleoside phosphoramidites with suitable nucleobase protection; (3) capping of the 5′-OH group of the unreacted starting material; and (4) oxidation to convert the phosphite triester (P^{III}) into the phosphate triester (P^{V}) backbone.[37]

For the branched RNA templates (Scheme 1), an asymmetric non-nucleoside branchpoint phosphoramidite monomer with orthogonal DMT and levulinyl (Lv) protecting groups was added to the RNA synthesis cycle for the controlled, regioselective addition of each (up to three) RNA strand from the branchpoint synthon.[38] The solid phase synthesis of V- and Y-shaped branched RNA templates (Scheme 1A) involves the incorporation of the branchpoint phosphoramidite (0.15 M, 12 min) at the 5′-end of the RNA strand, followed by decyanoethylation (2 : 3 v/v triethylamine in acetonitrile (NEt_3 : ACN), 90 min) prior to the removal of the branchpoint DMT group to prevent potential RNA strand isomerization and/or scission during the next RNA synthesis from the branchpoint moiety.[39] The second RNA strand was capped (acetic anhydride in pyridine, Ac_2O : pyr, and *N*-methyl imidazole in tetrahydrofuran, *N*-Me imidazole : THF) at the 5′-end of the V-shaped RNA template to prevent further elongation or functionalization of the template strand. To remove the levulinyl (Lv) protecting group,[40] hydrazine hydrate buffered in pyridine and acetic acid (0.5 M NH_2NH_2-H_2O : pyr : HOAc, 20 min) was used to selectively free the branchpoint OH group for completion of the V-shaped RNA templates or extension of the third RNA strand from the branchpoint position for the synthesis of Y-shaped RNA templates.

For fluorochrome (fluorescein isothiocyanate (FITC) or coumarin (CM)) labelling of RNA templates (Scheme 1B), a monomethoxytrityl (MMT)-protected amino hexamethylene phos-

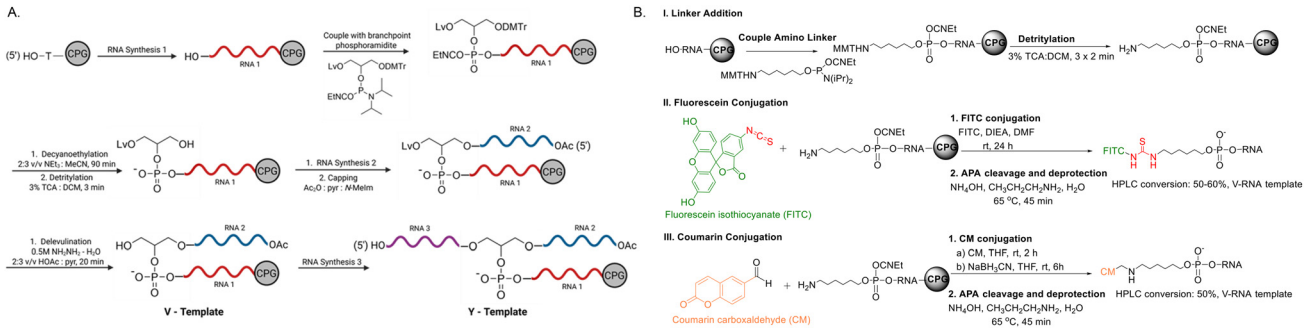

Scheme 1 Solid-phase synthesis strategy. (A) Asymmetric branch RNA synthesis. (B) Fluorescent labelling of V-shaped RNA templates.

phoramidite linker was added using solid phase RNA synthesis procedures (0.15 M, 12 min) at the branchpoint OH group for the V-shaped templates. The alkylamino linker required additional (2–3) detritylation steps to complete removal of the MMT group prior to bioconjugation. The RNA templates for FITC or CM labelling were selected for close proximity FRET biosensing applications,[36] to confirm hybrid structure formation and stability during the assembly process. For example, in the purported square nanostructure the FITC label was incorporated in the V-shaped RNA template strand (A75A78) and the CM label in the A94S78 strand. A FITC-labelling procedure was adapted from the literature (Scheme 1B),[29,32] to directly couple FITC to the alkylamino linked RNA templates. Overnight reaction of support-bound RNA templates yielded good (50–60%) conversions to FITC-labelled V-shaped RNA templates, following cleavage, deprotection and HPLC analysis. For CM-labelling onto the alkylamino linked RNA templates, a literature-based reductive amination procedure was used (Scheme 1B).[41] In this bioconjugation strategy, the alkylamino-linked RNA templates bound to the solid support were initially reacted (4–6 h) with coumarin carboxaldehyde to form the imine intermediate, which was subsequently reduced *in situ* following the addition of sodium cyanoborohydride to yield the CM-labelled RNA templates following an overnight reaction. Cleavage, deprotection and analysis by HPLC confirmed good (~50%) conversion for the CM-labelled V-shaped RNA templates. Of note, the unlabelled RNA templates were deprotected using ammonium hydroxide and aqueous 40% methylamine (50 : 50 v/v, AMA), while the fluorophore labelled templates were treated with ammonium hydroxide : propylamine : H_2O (2 : 1 : 1 v/v/v, APA) to prevent degradation of the fluorophore.[42] Following cleavage and deprotection of the RNA templates from the solid support, samples were desilylated to remove the 2′-TBDMS RNA protection.

Following solid-phase synthesis, cleavage and deprotection, the crude RNA templates were analysed and purified by Reverse-Phase Ion-Pairing High Performance Liquid Chromatography (RP IP HPLC) with ≥90% purities with identities confirmed by electrospray ionization mass spectrometry (ESI MS) according to the expected mass : charge ($m : z$) ratios for the RNA sequences synthesized in this study (SI, Table S2 and Fig. S1–S15). Furthermore, UV-Vis spectroscopic analysis was used to quantify the optical density (OD) values and molar concentrations of the RNA templates for characterization and biological studies of siRNA nanostructures (SI, Table S2 and Fig. S19–S23).

Characterization of multifunctional siRNA nanostructures

Native polyacrylamide gel electrophoresis (PAGE) was performed to evaluate the propensity for hybridization and assembly of RNA templates into well-retained, higher-ordered RNA (nano)structures (Fig. 2A–D and SI, Fig. S16–S18). The hybridization and assembly protocol for the proposed square-shaped nanostructure involved combining stoichiometric equivalent nanomolar quantities of four complementary V-shaped RNA templates (A75A78, A94S94, S75A170, S94S170), each composed of 39 nucleotides, corresponding to a 156 nucleotide length sequence. Optimization of RNA hybridization and assembly was tested in three different buffer conditions – phosphate buffered saline (PBS, 1 mL, 100 mM Na_3PO_4, 150 mM NaCl, 1 mM EDTA, pH 7.5), Tris buffer (1 mL, 10 mM Tris–HCl, 50 mM NaCl, 1 mM EDTA pH 7.6) or HEPES buffer (1 mL, 100 mM CH_3COOK, 30 mM HEPES, pH 7.5) – to produce hybrid dsRNA structures that template the assembly of higher-ordered (nano)structures. The complementary RNA templates were initially denatured (95 °C, 5 min), slowly cooled to room temperature for 2–3 h and subsequently stored overnight in the fridge (4 °C) to complete the hybrid duplex formation and assembly of stable, discrete RNA nanostructures. The samples were loaded onto a native 20% PAGE gel and resolved, which revealed stable assembly of the RNA templates into retained, higher-ordered structures across all buffer conditions (and to a lesser extent in H_2O, Fig. 2A and SI Fig. S16 and S17). The observed discrete bands for the presumed square-shaped assemblies were significantly more retained than those of the oligonucleotide ladder (20–100 nucleotides), V-shaped templates and linear RNA sequences used as controls, in their single-stranded and hybrid forms, without visible detection of any leftover unassembled V-shaped templates, indicating a complete RNA assembly process. The hybridization of the FITC- and CM-labelled V-templates into the expected square-shaped assembly was also evaluated by native PAGE (Fig. 2C and D and SI, Fig. S17). The square-FITC assembly yielded a band with electrophoretic

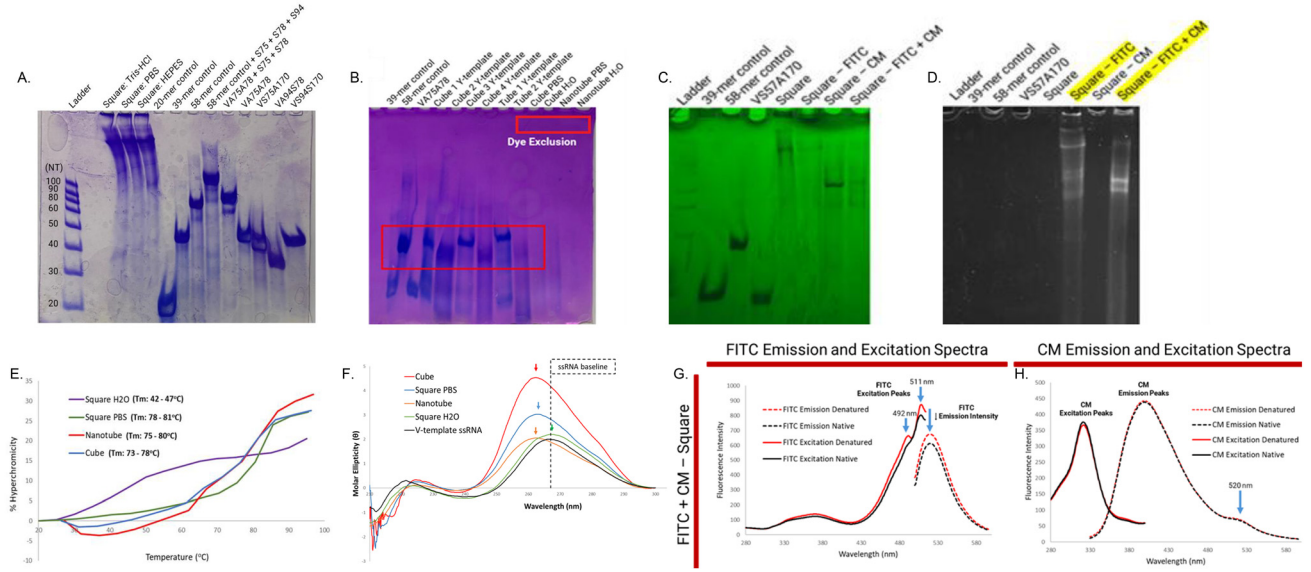

Fig. 2 Characterization of RNA structure, assembly and photophysical properties. Native (14–20%) PAGE of control (ssRNA, dsRNA, V-, Y-shaped RNA templates) and hybrid RNA assemblies into the proposed (A) square, (B) cube- and tube-shaped structures, (C and D) with and without (FITC and CM) fluorochromes formulated in H_2O or buffer (PBS, Tris or HEPES). Gels imaged under (A and B) Stains-All™, (C) low-UV (λ_{max}: 254 nm), and (D) high-UV (λ_{max}: 450 nm), displaying FITC fluorescence in the highlighted samples. (E) Thermal denaturation (T_m) curves and (F) CD spectra of the RNA hybrid duplex structures (1 μM) in H_2O and PBS. FRET biosensing of (G) FITC- and (H) CM-labelled RNA square samples (1 μM in PBS) in native (22 °C) and denatured (95 °C) forms, represented by the fluorescence excitation and emission spectra. The FITC excitation and emission wavelengths were set at λ_{ex} = 492 nm and λ_{em} = 520 nm. The CM excitation and emission wavelengths were set at λ_{ex} = 320 nm and λ_{em} = 420 nm.

mobility on the gel comparable to that of the unlabelled square sample formulated in PBS, indicating that the FITC V-shaped RNA template did not disrupt the hybridization efficiency of the assumed square-shaped assembly. However, the CM-labelled square-shaped sample yielded a less retained band on the gel, suggesting that the CM-labelled V-shaped RNA template may impact the hybridization efficiency of the assembled structure. In the hybridized, assembled form the combination of FITC and CM labelled V-shaped RNA templates formulated in PBS buffer (square FITC + CM) formed discrete, higher-ordered structures with retained electrophoretic mobility on the gel. However, the square-FITC + CM band appeared slightly less retained on the gel compared to the square (PBS) and square-FITC samples. This suggests that the CM and FITC could impact the RNA hybrid assembly formation of the desired square-shaped (nano)structure.

The hybridization of four (A75A75A75, S75S78S94, A170A94S75, S170A78A75) and two (A75A78A94 and S75S78S94) complementary Y-shaped RNA templates was conducted as described above for the square-shaped RNA assembly and was expected to produce the presumed cube and tube-shaped (nano)structures, respectively (Fig. 2B). The hybridization and assembly properties of the purported (nano)cube sample were evaluated on a native 14% PAGE gel in PBS and water (SI, Fig. S18). A retained band was detected on the gel with no apparent differences in electrophoretic mobilities in the PBS and H_2O formulation, without visible detection of any leftover unassembled V-shaped templates, indicative of stable hybridization for assembly of higher-ordered structures. Interestingly, with a Stains-All™ treated gel, the cube samples did not stain, indicative of dye exclusion from the assembled siRNA (nano)structure, while the single-stranded linear RNA and Y-shaped template controls were effectively stained (Fig. 2B and SI, Fig. S18b). A similar outcome was observed with the formation of the proposed nanotube assembly on native (14%) PAGE analysis (Fig. 2B and SI, Fig. S18). The nanotube assembly was expected to be lengthy and extensive, formed upon combination of the complementary Y-shaped RNA templates (A75A78A94 and S75S78S94) to scaffold an intricate, elongated (nano)structure. The proposed nanotube was difficult to visualize on the gel, yielding a faint streaking appearance under UV-shadowing, and dye exclusion with Stains-All™ staining, likely due to the formation of higher-ordered, continuous structural assemblies without any remaining unassembled Y-shaped templates (SI, Fig. S18). This outcome suggests that the assembled (cube- and tube-shaped) (nano)structures may potentially prevent dye binding to RNA, as also observed in our previous work, which showed weak Stains-All™ detection of various RNA nanostructures formulated from the assembly of synthetic V- and Y-shaped branched RNA templates.[28] This phenomenon is characteristic in other, higher-ordered hybrid assemblies of nucleic acids, including branched dsDNA junction motifs, which displayed Stains-All™ dye exclusion from the dsDNA and selective dye-binding interactions at branchpoint junctions.[43] These studies serve as additional experimental evidence of dye-exclusion or weak Stains-All™ detection in these types of branched supramolecular nucleic acid assemblies. Of significance, the native and

functionalized V- and Y-shaped RNA templates produced higher-ordered assemblies on native PAGE for (supra)molecular structure and photophysical characterization studies.

Following the PAGE analysis, the thermal stability of the hybrid double-stranded (duplex) siRNA secondary structures that template the assembly of higher-ordered supramolecular (nano)structures was evaluated by thermal denaturation (Fig. 2E). The melting temperatures (T_m) at the midpoint of the melting curves representing 50% conversion from double-stranded to single-stranded RNA were used to assess the most thermodynamically stable hybrid duplex siRNA structures in each (square, cube and tube) formulation. The thermal hybrid duplex stability of the unlabelled square sample was tested in H_2O and PBS to compare the effects of the buffer conditions on hybridization stability, which also impacted assembly, according to the native PAGE results (Fig. 2A and SI, Fig. S17). A notable difference was observed in the melting temperatures for the square sample hybridized in H_2O (T_m: ~42–47 °C), compared to PBS (T_m: ~78–81 °C). This outcome underscores the stabilizing ionic strength effect of the buffer by reducing the electrostatic repulsion of polyphosphate backbones while promoting stable base-pairing interactions in RNA secondary structures, which are otherwise weakened under low-salt conditions such as in pure water.[44,45] Similarly, the purported cube-shaped (nano)structure assembly formulated in PBS maintained a thermally stable hybrid duplex assembly (T_m: ~73–78 °C). These data also aligned with the thermal stability of the putative nanotube assembly (T_m: ~75–80 °C). These results confirm that the hybrid siRNA duplex structures have thermal stability that can be used to template the assembly of higher-ordered supramolecular (nano)structures.

Circular dichroism (CD) spectroscopy was used to investigate the secondary structures of the siRNA hybrid duplexes in the assembled (nano)structure (square, cube and tube) samples compared to ssRNA controls (Fig. 2F). The CD spectra of the V-shaped ssRNA template A75A78 displayed a broad maximum in molar ellipticity near 270 nm and a broad minimum near 240 nm consistent with the expected CD profile of ssRNA.[46] Interestingly, the square-shaped formulation in pure H_2O exhibited a nearly identical CD signature to the ssRNA control, suggesting a significant proportion of unpaired or weakly hybridized complementary template strands (A75A78, A94S94, S75A170, and S94S170). This observation correlates with the native PAGE (Fig. 2A and SI, Fig. S17) results and with the thermal denaturation data (Fig. 2E), which showed markedly lower thermal stability for hybrid duplex formation for this sample in H_2O (42–47 °C) *vs.* PBS (78–81 °C). Notably, all PBS formulated samples (square, cube, and tube) exhibited a lower-UV shift in molar ellipticity maximum to about 260 nm and a negative minimum to near 235 nm, characteristic of dsRNA *vs.* ssRNA, and for the characterization of A-form right-handed helical secondary structures.[46] These results confirm that the PBS-formulated assemblies were based on stable hybrid dsRNA A-type helices, which remain a functional requirement for siRNA processing activity *via* the RNAi mechanism.[47]

The photophysical properties of the fluorochrome (FITC and CM) labelled dsRNA assemblies were analysed using fluorescence excitation and emission spectra collected under native (22 °C) and denatured (95 °C) conditions (Fig. 2G and H). It was expected that under native RNA assembly conditions, the fluorescent reporters (CM and FITC) may undergo notable changes in photophysical properties (*i.e.*, intensity and wavelength shifts) that would be detectable in the excitation and emission spectra, when compared to fluorochrome-labelled RNA in the denatured ssRNA form. The singly-labelled RNA (nano)structures (CM-square and FITC-square) were analysed with FITC excitation and emission wavelengths set at λ_{ex} = 492 nm and λ_{em} = 520 nm (SI, Fig. S24a).[48] The excitation and emission wavelengths for CM were set at λ_{ex} = 320 nm and λ_{em} = 420 nm (SI, Fig. S24b).[49] The excitation and emission wavelengths for each fluorochrome were established separately by UV-Vis and fluorescence spectroscopy (SI, Fig. S21 and S25). The square-FITC and square-CM singly labelled samples did not display significant changes in the excitation and emission spectra in the native and denatured forms (SI, Fig. S24). However, for the CM-labelled square sample, a noticeable, yet small decrease in the excitation and emission intensities in the denatured form was observed. Alternatively, the CM-labelled square assembly generated a small but detectable increase in excitation and emission intensities in the native *vs.* denatured forms. These data suggest that the observed changes in CM optical properties may be due to the dynamic RNA structure assembly process from the native (hybrid) to denatured (single-stranded) forms.

The combination of FITC and CM-labels incorporated into the assumed square-shaped RNA assembly was used for fluorescence resonance energy transfer (FRET) biosensing applications (Fig. 2G and H). Coumarin and fluorescein have been used as a donor–acceptor pair for fluorescence energy transfer, providing structure and biophysical characterization of nucleic acids.[36] The FITC and CM labels were installed on adjacent branchpoint positions within the square-shaped RNA assembly (Fig. 1A) using the requisite V-shaped RNA templates (FITC-A75A78, A94S94, CM-S75A170, and S94S170), which provides a close proximity effect for FRET signalling. The excitation and emission spectra were collected for FITC and CM-labelled templates alone (SI, Fig. S25) and in the presumed square-shaped RNA assembly under native (22 °C) and thermal denaturation (95 °C) conditions (Fig. 2G and H). A pronounced FRET pair effect was observed for FITC and CM in the assembled RNA formulation in the excitation and emission spectra. The strong FITC excitation peak at λ_{ex} = 486 nm underwent splitting and a notable red shift in wavelengths, which produced two new peaks at λ_{ex} = 492 and 511 nm, with decreasing intensities in the native *vs.* denatured forms. Similarly, a noticeable drop in the FITC emission intensity was observed at λ_{em} = 520 nm for the sample in the native *vs.* denatured forms, suggesting a fluorescence quenching effect for FITC in the annealed, assembled formulation. Alternatively, an increase in FITC excitation and emission was observed under thermal denaturation (95 °C), consistent with the transition from the

annealed (hybrid) to denatured (single-stranded) form. This outcome suggests that as the Förster distance between the FITC and CM is increased in the denatured form, a decrease in the Förster energy transfer occurs between FITC and CM, causing a gain in FITC emission intensity with less energy transfer to CM.[50] However, in the FRET pair (native) assembly, upon FITC excitation, the fluorescence energy is transferred to CM, resulting in the observed decrease in FITC emission intensity. Based on the FITC emission data in native *vs.* denatured forms of the square shaped RNA assembly, the distance-dependent FRET efficiency (E = 1 − (F_native/F_denatured)) within the FITC and CM FRET pair was calculated (E = 0.09), and it was found to be consistent with the observed distance-dependent decreases in the apparent FRET efficiencies (E_{app} = 0.6–0.3) in the CM and FITC donor–acceptor pair in DNA duplexes with increasing (10–16) base pairs, compared to the lengthier 19 base-pair RNA duplexes within the square shaped assembly.[36] Furthermore, the red-shifted peak splitting observed in the FITC excitation spectra (Fig. 2G) suggests a prolonged CM effect on the photophysical properties of FITC. The presence of CM near FITC causes its excitation at lower photon energy with longer (red-shifted) wavelengths, enabling distance dependent non-radiative energy transfer *via* dipole–dipole coupling.[50] This leads to a decrease in the fluorescence emission intensity of FITC in the emission spectra (Fig. 2G). The appearance of a FITC emission peak at λ_{em} = 520 nm in the CM emission spectra (Fig. 2H) may be due to energy absorption by CM (from FITC) and subsequent emission in this characteristic FRET sensing event in the donor–acceptor pair.[36] These results confirm the fluorescence energy transfer within the FRET pair, which delineates a dynamic assembly process of the putative square-shaped RNA nanostructure under native and thermal denaturation conditions.

Dynamic light scattering (DLS) analysis provided complementary characterization data for the proposed RNA nanostructures (Table 1). The square-shaped sample correlated with a low polydispersity (PDI: 0.162) measurement, which supports the observation of uniform, monodisperse nanoparticles by TEM (Fig. 3). The particles also displayed a larger effective hydrodynamic diameter (279 ± 93 nm) in pure water compared to PBS (161.38 ± 16.07 nm). The larger sample sizes (in H_2O and compared to TEM analysis) could be due to the hydration sphere that increases particle size measurements during DLS and the ionic strength from buffer that condenses (nano)particle formulations.[51] Furthermore, all samples in PBS displayed consistent negative value zeta potential measurements (~−30 to −40 mV), contributed partly due to the surface charge density of the polyanionic phosphate groups. However, the square-shaped sample measured in low-conductivity H_2O led to unreliable zeta potentials (~−60 mV), likely due to the inability to form a stable electrical double layer in charged particles for accurate measurements.[52] Importantly, all samples produced zeta potentials <−30 mV and were considered electrostatically stable, as strong repulsive forces of ionic particles in suspension prevent colloidal aggregation.[52]

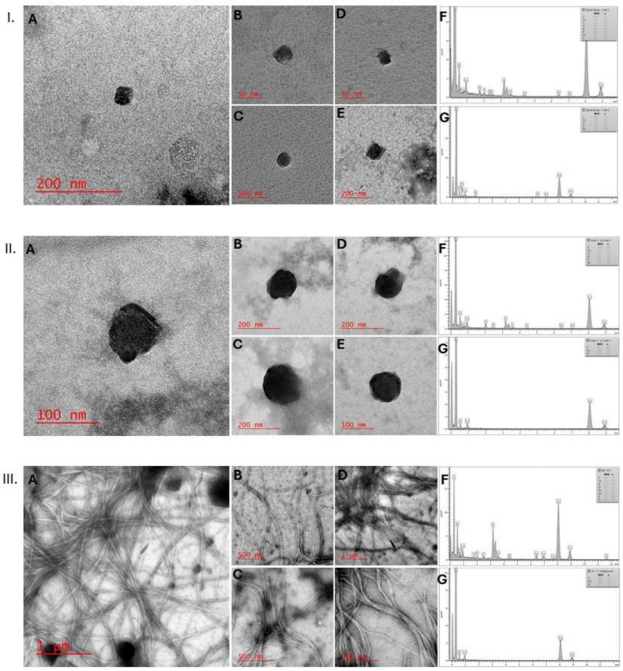

Fig. 3 TEM images and EDX spectra of the RNA nanostructures (1 μM in H_2O): (I) squares (A–G), (II) cubes (A–G), and (III) tubes (A–G).

Transmission Electron Microscopy (TEM) was next performed to visualize the morphology of the RNA nanostructures (Fig. 3).[53] The samples (square, cube and tube) were prepared in H_2O (1 μM) deposited on carbon-coated grids and dried prior to TEM imaging. The samples were formulated in pure water, as the presence of salt crystals from PBS interfered with the visualization of (nano)particles.

The RNA nanostructures were stable at room temperature (22 °C) and visualized effectively by TEM. Energy dispersive X-ray (EDX) spectroscopy was performed during the TEM analysis to confirm the presence of RNA. Phosphorous (P) was regularly detected in the EDX spectra of all samples, supporting the presence of phosphate groups in the RNA backbone (Fig. 3F). This EDX analysis confirmed the RNA composition of the nanostructures rather than background (salt) contaminants or artefact particles on the TEM grids (Fig. 3G). The observed TEM images for all samples revealed well-defined, monodisperse nanostructures amenable to (supra)molecular shape analysis and dimensional size measurements for the characterization of discrete RNA nanostructures (Table 1). The

Table 1 Characterization of RNA nanostructures

Sample	Size[a] (nm ± std)	Zeta potential[b] (mV ± std)
Square	47.39 ± 10.87	−41.18 ± 8.78
Cube	137.97 ± 34.82	−40.30 ± 4.79
Tube[c]	30.78 ± 7.98	−33.66 ± 2.98

[a] Characterized by TEM. [b] Characterized by DLS. [c] Width measurements of the observed internal cavities and length measurements (200 nm–10 μm) of the elongated nanotubes.

square-shaped RNA assembly (Fig. 3-I, A–E) revealed uniform, monodisperse small-sized (47.39 ± 10.87 nm) nanostructures. The cube-shaped supramolecular assembly was also confirmed (Fig. 3-II, A–E), yielding uniform nanostructures with larger size measurements (137.97 ± 34.82 nm), compared to the square-shaped nanostructures. However, the 3D-cubic geometry was visible from the TEM images, which appeared to contain overlapping layers of RNA assemblies in a cubic-type morphology with consistent size and shape with minimal aggregation. The RNA nanotube was also visualized by TEM imaging (Fig. 3-III, A–E), with a long entangled network of tubular nano-to-micrometre size structures, with consistent width (30.78 ± 7.98 nm) and extensive length measurements ranging from 200 nm to over 10 μm. The higher-ordered tubular RNA assemblies were much larger than the observed RNA nano-squares and cubes (Fig. 3 and Table 1), as well as other known RNA nanostructures previously reported.[28] The remarkable RNA nanotubes stemmed from the hybrid assembly of only two complementary Y-shaped RNA templates (A75A78A94 and S75S78S94), which scaffolded the elongation of these incredibly long, intricate, yet well-defined RNA supramolecular architectures. In addition to the well-defined RNA nanostructures (Fig. 3), larger aggregates were apparent on a larger scale (500 nm to 1 μm) magnification, providing a broader field of view, with nanoparticles observed on a smaller scale (100–200 nm) magnification (SI, Fig. S27). Moreover, accurate supramolecular characterization and precise size measurements of 3D RNA architectures can be challenging with TEM. Thus, atomic force microscopy (AFM) was used for supplemental structure characterization and size and height measurements of the RNA nanostructures (SI, Fig. S28 and Table S5). The AFM analysis for the square sample (SI, Fig. S28-I and Table S5) produced many discrete and monodisperse single particles of small nanoscale sizes (50–60 nm) and height dimensions (25–30 nm) consistent with the morphology and sizes of the nanoparticles analysed from the TEM images (Fig. 3-I). The AFM analysis of the cube sample (SI, Fig. S28-II and Table S5) indicated various separate particles and aggregated clusters. The single nanoparticles were found to be of comparable (55–65 nm) sizes to the nanosquares. However, the reduced height measurements tabulated for single particles (2–5 nm) and aggregated forms (~10 nm) suggest structural collapse for this sample during the drying and analysis processes.[53,54] In addition, the AFM images revealed larger (130–170 nm) multi-particle clusters for this sample, which also showed a tendency to aggregate into multi-particle clusters of comparable sizes and morphologies during the TEM analyses (Fig. 3-II and SI, Fig. S27). The AFM analysis of the tube sample revealed very long (10–20 μm) interconnected networks of fibrils, with notable height (~30 nm) and thicker width (150–200 nm) measurements (SI, Fig. S28-III and Table S5), compared to the entangled filaments detected from the TEM imaging (Fig. 3-III). Moreover, upon sample magnification, excessive clustering of smaller single nanoparticles, ~100 nm in size and ~30 nm in height, was apparently directly involved in the formation of fibrillar aggregates. Thus, the appearance of the long, entangled filaments detected by TEM and AFM is likely due to multiparticle clustering effects, which may stem from the template assembly process of the RNA square into tube-type structures. Of significance, these types of RNA assemblies hold great potential as slow-release carriers in drug delivery applications, particularly in extracellular microenvironments for cell surface engineering with RNA nanotechnology.[55] Furthermore, the geometry, modularity and potential for chemical functionalization make the observed RNA nanostructures promising candidates in nucleic-acid based biosensing and therapeutic applications.[56]

Biological properties of multifunctional siRNA nanostructures

Flow cytometry and confocal laser scanning fluorescence microscopy were next employed to evaluate the direct binding, cell uptake and intracellular localization of a FITC-labelled square-shaped RNA assembly within the human adenocarcinoma (A549) cell line. Flow cytometry was initially used to test RNA dependent cell binding activity in the absence and presence of Lipofectamine 3000™, an industry-standard cationic lipid transfection reagent commonly used for gene transfer activity in the A549 lung cancer cells (Fig. 4A–C).[57] A strong increase in the percentage (>90%) of fluorescently (FITC-RNA)-labelled cells from the total population of gated A549 cells was detected in the presence of Lipofectamine 3000™ (Fig. 4C). In the absence of the benchmark transfection reagent no population of fluorescently labelled cells was observed, akin to the control, no treatment conditions (Fig. 4A and B). This outcome underscores the importance of the transfection reagent in promoting the cell binding activity of the FITC-labelled RNA sample. This result aligns with our previous FITC-siRNA transfection studies,[29] as well as others describing the importance of cationic lipids in the formulation of lipid nanoparticles for the stable, safe and effective delivery of siRNA in challenging-to-transfect adherent cell lines.[58]

Confocal microscopy was next used to visualize the cell binding events of the FITC-labelled RNA square assembly with and without Lipofectamine 3000™ within the A549 cells (Fig. 4D and E). The confocal fluorescence microscopy images revealed the impact of FITC-labelled RNA binding activity (Fig. 4C) on A549 cellular uptake (FITC-green) and localization (cytoskeleton-actin stained with Alexa Fluor™ 647 Phalloidin, nuclei stained with DAPI) using the Lipofectamine-based transfection protocol (Fig. 4E) and without cell binding and uptake for the FITC-siRNA sample in the absence of the transfection reagent (Fig. 4B and D). The FITC-labelled RNA displayed widespread cell uptake and distribution in the A549 cells. The most pronounced intracellular localization was observed in the cytosol and perinuclear regions, consistent with the reported mechanism of Lipofectamine-based gene transfer activity.[59] Furthermore, a time-dependent (1 h *vs.* 4 h) cell uptake and colocalization study was performed for the FITC-labelled siRNA square transfected with Lipofectamine 3000™ (Fig. 4F). The A549 cells were DAPI (nuclei; blue) and LysoTracker™ (endolysosomes; deep red) stained and visualized by confocal microscopy. Qualitative and quantitative ana-

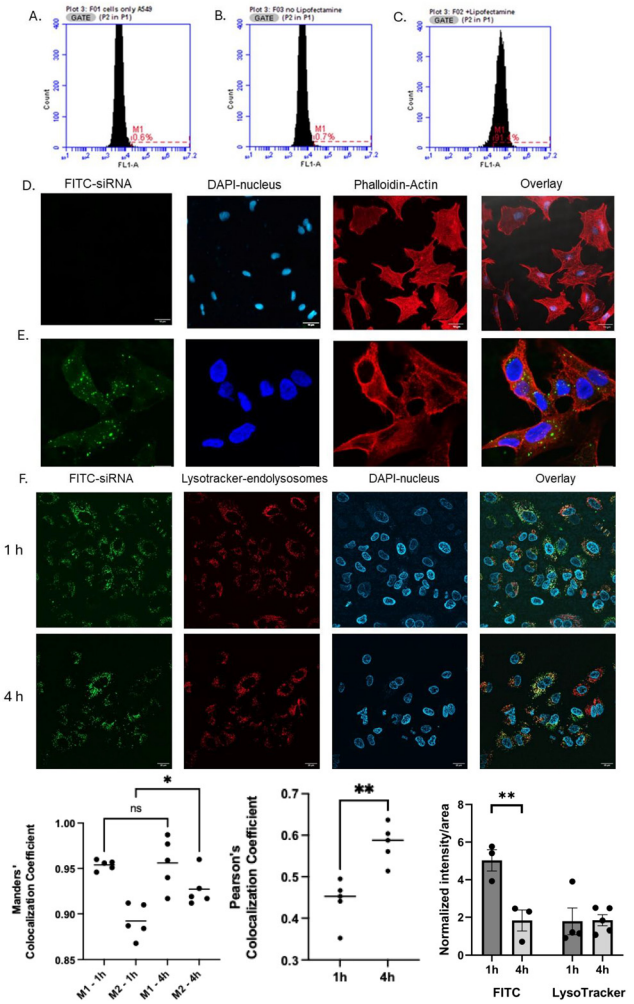

Fig. 4 Cell binding and uptake of a FITC-labelled square-shaped RNA assembly within the human adenocarcinoma (A549) cell line in the absence and presence of Lipofectamine 3000™. Flow cytometry data showing the gated population of A549 cells with (A) no treatment, (B) FITC-labelled siRNA alone and (C) FITC-siRNA (25 nM) and Lipofectamine (6 μL) in PBS incubated for 1 h at 37 °C. Confocal microscopy images showing FITC-siRNA (25 nM) cell uptake and intracellular localization in the absence (D) and presence (E) of Lipofectamine transfection in OPTIMEM for 4 h at 37 °C. Scale bars are set at 10 μm. (F) Confocal microscopy of cell uptake and colocalization of FITC-siRNA with Lysotracker™ Deep Red stain following Lipofectamine-based transfections. Scale bars are set at 20 μm. Colocalization was quantified in the FITC and the Lysotracker channels using Manders' coefficients (M_1 and M_2) and Pearson's correlation coefficients showing progressive time-dependent (1–4 h) correlations of FITC and Lysotracker. Values are displayed as individual data points with mean ± SD. Statistical comparisons between 1 h and 4 h were performed using a two-tailed test (unpaired), with significance defined at $p < 0.05$. Statistical analysis of the normalized differences in mean fluorescence intensity (MFI) values plotted as mean MFI ± SEM for FITC and Lysotracker (1–4 h) based on one-way ANOVA significance analysis that included the control data, which was normalized to Tukey's *post hoc* for multiple comparisons, with $p < 0.01$.

lyses of the (FITC + LysoTracker) overlaid images demonstrated a time-dependent (1–4 h) correlation in the FITC-siRNA endolysosomal colocalization, combined with a decrease in FITC mean fluorescence intensity (MFI) values, suggesting endolysosomal siRNA uptake into the cytosolic and perinuclear regions of the A549 cells. Moreover, FRET-based RNA nanostructures have been studied in intracellular imaging and biosensing applications.[19] Fluorescence-based imaging analysis was conducted in the A549 cells to investigate cell-based FRET biosensing for the FITC and CM-labelled square-shaped RNA assembly (SI, Fig. S29). Fluorescence imaging analysis revealed strong fluorescence signalling, across both channels of detection for the FRET-pair FITC- and CM-labelled A549 cells upon Lipofectamine-based transfection of the dual FITC + CM-labelled square shaped RNA assembly (SI, Fig. S29-A). In comparison, the square-FITC- and square-CM singly labelled siRNA samples showed fluorescence signalling in their respective channels (SI, Fig. S29B and C). However, some crossover in fluorescence signalling due to the spectral overlap of CM (SI, Fig. S24, λ_{ex} = 320 nm) and FITC (SI, Fig. S24, λ_{max} = 350 and 490 nm) was also observed during the analysis. This phenomenon hinders any accurate quantitative analysis of the differences in mean fluorescence intensity (MFI) values across the various samples in the FITC and CM channels. Nonetheless, this qualitative fluorescence imaging analysis provides experimental evidence of the intracellular detection of biosensing events in the A549 cells for the FITC + CM-labelled square shaped RNA assembly.

However, the RNA cube and tube samples and their prerequisite RNA templates were not fluorescently labelled, thereby preventing their bioanalysis by fluorescence-based flow cytometry and confocal microscopy. To fill this gap, Raman microspectroscopy was used for direct spectroscopic characterization of biomolecules in their unlabelled (label-free) form.[60] Furthermore, this technique also enables live cell microscopy imaging, analysis of chemical compositions and (intra)cellular distributions of biomolecules and synthetic nanoparticles in biological systems, such as organelles.[61] This advanced bioanalytical technique has also been used for single cell analysis of RNA content and expression profiles in living cells,[62] making it particularly relevant and well-suited to the characterization of the RNA nanostructures described in this study. Raman spectroscopic analysis of the RNA nanosquare, nanocube and nanotube samples in their label free form and free from cells yielded consistent Raman spectra across all samples (SI, Fig. S26). Characteristic Raman spectral peaks for RNA content were detected at around 600 cm^{-1}, related to the purine and pyrimidine base residue orientations in RNA assemblies, followed by a smaller peak at ~800 cm^{-1} (nanocube) and a more intense broad peak between 850 and 950 cm^{-1} (nanosquare and nanotube), which were respectively assigned to the phosphodiester (OPO) symmetrical stretching and to the ribose-phosphodiester backbone stretching as key fingerprint region (800–950 cm^{-1}) markers for the identification of the A-type helical conformation of dsRNA, and with all samples displaying an intense Raman peak at ~1100 cm^{-1}, as a prominent RNA band assigned to the phosphodioxy (PO_2^-) symmetrical stretch.[63] Live A549 cell imaging and characterization by Raman microspectroscopy of the

unlabelled RNA (square, cube and tube) nanostructures following Lipofectamine-based transfection revealed the same characteristic Raman spectra for all samples when compared to the analysis of their free forms (Fig. 5 and SI, Fig. S26). Furthermore, the Raman spectra from the RNA nanostructures were clearly distinct and more pronounced from the spectral analyses of intracellular (*i.e.*, nuclei and organelles) regions of the A549 cells. Therefore, this analysis was used to distinguish and characterize the chemical composition of the RNA nanoparticles from the biomolecules and intracellular compartments present in the A549 cells. Live cell imaging obtained from the Raman chemical component mapping of spectral datasets confirmed the biochemical heterogeneity of the RNA nanoparticles from the cellular components, with distinct intracellular spatial distributions detected for the RNA nanoparticles in the A549 cells. The combined A549 cell binding and intracellular (cytosolic and perinuclear) localization (Fig. 4 and 5) of the siRNA nanostructures makes them amenable to transfection studies to investigate the impact of GRP silencing on the anti-cancer effects of the A549 cells.

Our research has focused on the siRNA-based inhibition of stress-related chaperone proteins (the GRPs for promoting anti-cancer cell cycle arrest and antiproliferative activities resulting in tumor toxicity (apoptosis)).[27–32] In this contribution we were driven to potentiate the anti-cancer responses in synergy by silencing all main GRPs, GRP75, GRP78, GRP94, and GRP170, in lung cancer. This tumor displays an addiction to GRP overexpression and oncogenic signalling associated with tumour growth and differentiation, metastasis, angiogenesis, and immune evasion, which also correlates with the evolution of chemoresistance.[64–68] Given the fundamental roles of the GRPs in oncogenesis, inhibition of *Grp* expression and impairment of GRP function in lung cancer with the multi-GRP silencing RNA nanostructures represents an innovative cancer intervention strategy against this complex and challenging-to-treat disease.

A preliminary dose-dependent (25 *vs.* 50 nM) siRNA transfection study in the absence and presence of Lipofectamine 3000™ was used to screen the knockdown effects of the multi-GRP targeting siRNA constructs *vs.* controls (SI, Fig. S30). The higher-dose (50 nM) siRNA treatment mitigated GRP-silencing and the absence of Lipofectamine abolished siRNA transfection, in alignment with the flow cytometry and confocal microscopy cell binding and uptake results (Fig. 4). In contrast, lower-dose (25 nM) administration of the siRNA constructs with Lipofectamine 3000™ demonstrated more pronounced GRP-knockdown effects (Fig. 6 and SI, Fig. S30). These outcomes also correlate with our previous work,[28] which demonstrated lower-dose siRNA transfection efficacy and specificity in the catalytic RNAi pathway. Furthermore, these results highlight the critical importance of the Lipofectamine-based transfection agent, enabling the transfection efficiency of the RNA nanostructures, as documented in our previous reports,[29] as well as others, describing the importance of cationic lipids for the delivery of siRNA in challenging-to-transfect adherent cancer cell lines.[58] The optimized transfection conditions (25 nM siRNA with Lipofectamine 3000™, Fig. 6) examined the impact of RNA nanostructure (square, cube and tube) treatment on GRP knockdown at the mRNA transcript and protein levels of expression, respectively, by reverse transcrip-

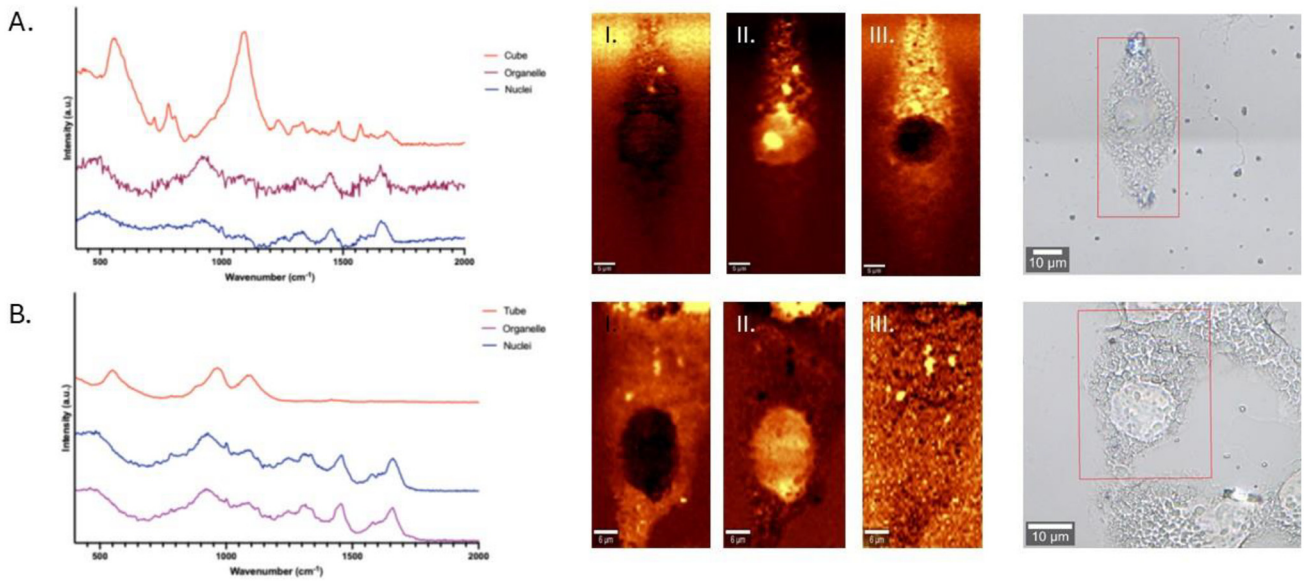

Fig. 5 Raman microspectroscopy analysis of the A549 cells treated with the Lipofectamine-based transfection conditions for the siRNA nanostructures (25 nM): (A) cube and (B) tube. Raman chemical component maps obtained through hyperspectral Raman imaging and True Component Analysis (TCA). Distinct spatial distributions of spectral components (I – "siRNA nanostructures"), (II – "nuclei"), (III – "organelles") reveal intracellular biochemical heterogeneity. The corresponding brightfield images show the cellular morphologies and the mapped acquisition areas (red rectangles). Raman analysis: scale bars are set at 5 μm; and brightfield images: scale bars are set at 10 μm.

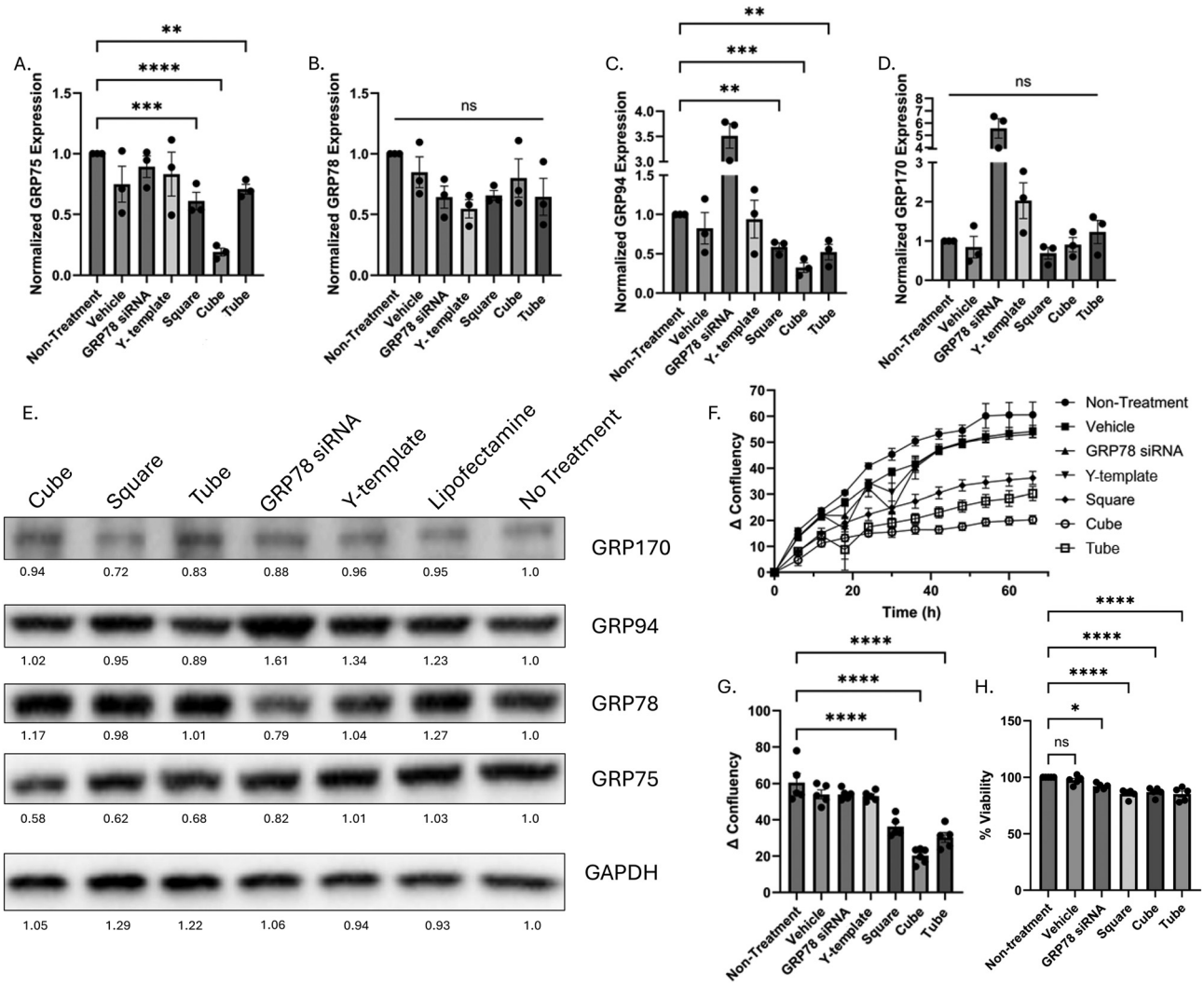

Fig. 6 GRP expressions in the A549 cells. siRNA transfections (25 nM) of the siRNA nanostructures (cube, square and tube) along with GRP78 siRNA, Y-template and vehicle controls with Lipofectamine 3000™ (6 μL) in DMEM cell culture media supplemented with 10% FBS over a 66 h period in a humidified incubator set at 37 °C with 5% CO_2. (A–D) RT-qPCR data and (E) western blots of GRP75, GRP78, GRP94, GRP170 and GAPDH (control housekeeping marker) used to normalize and quantitate mRNA and protein levels of expression. (F and G) Changes in A549 cells' confluency as an indicator of proliferative activity monitored in an Incucyte™ under the transfection conditions. (H) Cell viability data based on the resazurin (AlamarBlue™) assay of the A549 cells following siRNA transfections over a 48 h incubation period. Gene expression and confluency data representing at least three biological replicates ($N \geq 3$) are represented as mean values ± standard error about the mean (SEM). The statistical significance was determined in the GraphPad format using an ordinary one-way ANOVA with Dunnett's *post hoc* analysis (*$p < 0.05$, **$p < 0.01$, ***$p < 0.001$, ****$p < 0.0001$).

tion quantitative polymerase chain reaction (RT-qPCR) and western blot analysis. A direct comparison of the controls (no treatment, Lipofectamine vehicle, GRP78 siRNA and Y-shaped RNA template) *vs.* the Lipofectamine-based transfection of the RNA nanostructures (25 nM in DMEM, square, cube and nanotube) was used to evaluate the siRNA transfection efficiency in the A549 cell culture for 66 h at 37 °C. Isolation and quantitative analysis of the *Grp* mRNA transcript levels by RT-qPCR revealed a significant reduction in *Grp75* (Fig. 6A, 30–80%) and *Grp94* (Fig. 6C, 40–70%), along with a noticeable but non-significant decrease in *Grp78* (Fig. 6B, 20–35%) and to a lesser extent *Grp170* (Fig. 6D, 10–30%) mRNA transcript levels across the RNA nanostructure treatment conditions and absent in the nanotube formulation. The observed changes in mRNA *vs.* protein levels of GRP expression are correlated with the catalytic RNAi mechanism of siRNA gene silencing activity. A direct impact occurs on the mRNA transcript followed by later, variable effects observed at the protein levels of expression. The variable GRP expressions may be due to extended protein turnover rates, molecular crosstalk linked to compensation mechanisms, protein metabolism, post-transcriptional/translational modifications and regulatory events that offset a direct correlation between mRNA transcript and protein levels of expression.[71] Of significance, the RNA cube assembly gave the

most potent (70–80%, *Grp*75 and *Grp*94) knockdown effects, with the most significant impact on *Grp*75 likely due to the excess (6×) incorporation of GRP75 siRNA. Interestingly, *Grp78* silencing (with control GRP78 siRNA) led to significant increases in *Grp94* (Fig. 6C, >3-fold) and *Grp170* (Fig. 6D, >5-fold) mRNA transcript levels, suggesting a compensation effect in the upregulation of these chaperones that may also dampen the *Grp* knockdown responses of the RNA nanostructures. A similar trend was observed at the protein levels of expression by western blot (Fig. 6E). Downregulation of GRP78 (~20%, with GRP78 siRNA control) resulted in significant upregulation of GRP94 (~60%), which diminished the overall GRP knockdown for the RNA nanostructures. A similar GRP compensation effect was observed in other cancer cell lines subjected to cellular stress *via* GRP78 knockdown, leading to concomitant GRP94 upregulation in an adaptive mechanism that aims to restore cellular homeostasis under stress induction to sustain cancer survival.[69,70] Despite this adaptive resistance mechanism to GRP knockdown, the RNA nanostructures led to notable knockdown effects on GRP75 (30–40%) and GRP170 (20–30%), with the cube and square assembly generating the largest drop in GRP75 (40%) and GRP170 (30%), respectively, and to a lesser degree GRP78 and GRP94 (<10%). Thus, co-silencing the GRPs with the RNA nanostructures mitigates the GRP compensation effects observed with the control GRP78-targeting siRNA. The multi-GRP silencing RNA nanostructures can overcome the adaptive resistance mechanism to singly-targeted GRP(78) knockdown and then transition tumors from a pro-survival phenotype to a state of pronounced cancer cell death.[28]

In this study, the RNA nanostructures were used to examine the influence (if any) of GRP silencing on cell stress, (anti)proliferation and toxicity associated with lung cancer biology (Fig. 6). Interestingly, the most pronounced GRP silencing effects observed at the mRNA transcript (*Grp*75 and *Grp*94) and protein (GRP75 and GRP170) levels of expression with the RNA nanostructures also conferred a general maintenance of the master regulator of the ER stress chaperone (GRP78), suggesting an interplay between pro-survival and cell death outcomes under ER stress induction.[72,73] This biological outcome correlates sustained, late-stage ER stress, due to impaired GRP expression (Fig. 6A–E), with significant antiproliferative effects of the RNA nanostructures on the A549 cells (Fig. 6F and G). A cell viability/toxicity study (Fig. 6H) following siRNA transfections in the A549 cells was conducted with the resazurin (AlamarBlue™) cell viability assay that measures metabolic activity as an indicator of cell viability.[74] The siRNA nanostructures (square, cube and tube) triggered a significant reduction (15–20%) in A549 cell viability compared to the negative controls (<5%), no treatment and Lipofectamine-based vehicle conditions and to a greater extent relative to the GRP78 siRNA acting as a positive control (5–10%). These cell viability data correlate with the moderate effects of the siRNA nanostructures on GRP knockdown and antiproliferative activities (Fig. 6), in which GRP (down)regulation aims to maintain and/or restore the protective pro-survival phenotypes of lung cancer.[68,69,73]

Among the most potent RNA nanostructures, the cube-shaped RNA assembly produced the greatest GRP knockdown at the mRNA transcript (70–80%, *Grp*75 and *Grp*94) and protein (~40%, GRP75) levels of expression (Fig. 6A, C and E), likely due to the pronounced (6×) incorporation of GRP75 siRNA, which translated into the most significant (3-fold drop in confluency) antiproliferative activities (Fig. 6F and G) on A549 cancer cell growth inhibition that led to a marked reduction (15–20%) in lung cancer cell viability (Fig. 6H). This result highlights the important roles of the GRPs in the regulation of the pro-survival and antiproliferative phenotypes of lung cancer in the stressed, GRP-dependent tumor microenvironment.[68–70,75] The multi-GRP silencing RNA nanostructures function to overcome this adaptive resistance mechanism to singly-targeted GRP(78) siRNA knockdown while enhancing the anti-proliferative and toxicity effects in the A549 cells (Fig. 6F–H). This important biological outcome highlights the anti-tumor efficacy of the multifunctional RNA nanostructures, resulting in the discovery of a new nanotechnology for the advancement of cancer gene-silencing therapies against this challenging-to-treat type of lung cancer.

Conclusions

In conclusion, this research demonstrated the rational design and assembly of synthetic RNA templates into discrete, supramolecular siRNA nanostructures for cancer gene silencing applications. The new siRNA nanostructures expanded the repertoire of existing multifunctional siRNAs *via* the incorporation of synthetic (branchpoint) modifiers and fluorochrome units that enabled the study of the structural, photophysical and biological properties of RNA. The synthetic V- and Y-shaped branched RNA templates in their fluorochrome (FITC and/or CM) (un)labelled forms were effectively hybridized to their complementary RNA sequences that generated higher-order siRNA assemblies according to native PAGE. The FITC and CM labels were installed on adjacent branchpoint positions in the square-shaped RNA assembly to confirm the fluorescence energy transfer within the FRET pair, which revealed a dynamic assembly process of the square-shaped RNA nanostructure under hybrid and thermal denaturation conditions. Thermal denaturation (T_m) and CD spectroscopy were also, respectively, used to evaluate the siRNA hybrid stabilities and A-form helices required for RNAi activity. The siRNA hybrids assembled into discrete and well-defined nanostructures, which resembled square-, cube- and tube-shaped supramolecular assemblies according to TEM imaging and EDX analysis. The observed structural and photophysical properties of the siRNA nanostructures make them promising candidates in RNA-based biosensing and therapeutic applications. In lung (A549) cancer cells, the FITC-labelled RNA square with Lipofectamine 3000™ transfection was found to bind to and internalize within the A549 cells according to flow cytometry cell binding, confocal microscopy and Raman microspectroscopy cell uptake studies. Transfection of the

siRNA (square, cube and tube) nanostructures in the A549 cells produced significant GRP knockdown effects, detected at the mRNA transcript (RT qPCR) and protein (western blot) levels of expression. The most significant GRP silencing responses detected at the mRNA transcript (*Grp*75 and *Grp*94) and protein (GRP75 and GRP170) levels also sustained GRP78 expression, functioning as a key regulator of intracellular (ER) homeostasis, with important implications in the pro-survival and antiproliferative phenotypes of lung cancer. The multi-GRP silencing RNA nanostructures impaired the GRP expression levels, resulting in ER stress induction that promoted significant antiproliferative and toxicity effects on the A549 cells. Among the RNA constructs, the cube-shaped RNA assembly was the most effective. It produced the greatest GRP knockdown effects that led to the largest drop in A549 cell proliferative activity as an indication of cancer cell growth inhibition, which also translated into a significant decrease in cancer cell viability. This study highlights the important biological roles of GRPs in the maintenance of the pro-survival and proliferative phenotypes of lung cancer. Targeting the GRPs with the siRNA nanostructures represents a promising advancement in cancer gene-silencing therapies in resilient tumors that display a tendency to overexpress GRP. Future work is geared towards the introduction of nucleic acid modifications (*e.g.*, 2′-OMe RNA and 2′-F RNA) and payloads (*e.g.*, drugs) that improve siRNA knockdown efficacy and pharmacological properties while enhancing cancer cell toxicity for *in vivo* applications in tumor-bearing mouse models of lung cancer. Additional future work is dedicated to the development and optimization of cancer-targeted gene therapy. The application of cancer-cell targeting and penetrating peptides,[75] as well as aptamer ligands selected against cancer biomarkers and cellular targets,[76] is expected to overcome the toxicity and non-selective side effects of therapeutic gene delivery (*e.g.*, cationic lipid-based) formulations and conventional cancer therapy strategies.[77] This forms the basis of our current and future research objectives for the advancement of a safe and effective precision oncology strategy. In this study, a novel class of multifunctional siRNA nanostructures are reported for screening important (and multiple) oncogene targets for potential translational applications in cancer gene therapy.

Author contributions

M. S., J. O. and F. K. C. contributed equally to this work and conducted experimental investigations. M. R. and A. I. provided experimental assistance. W. G. W., B. C. M., and D. S. supervised, secured project funding, and compiled the manuscript. All authors have read and approved this manuscript.

Conflicts of interest

There are no conflicts to declare.

Data availability

The data supporting this article have been included as part of the supplementary information (SI). Supplementary information: experimental methods, LCMS and spectroscopic data, and additional characterization data. See DOI: https://doi.org/10.1039/d5bm01877c.

Acknowledgements

This work was gratefully supported by a Natural Sciences and Engineering Research Council (NSERC) Discovery Grant to D. S. (RGPIN-2024-05349) and a Discovery Horizons Grant to W. G. W. (DH-2025-00049). D. S. would also like to acknowledge the infrastructure funding from the Canada Foundation for Innovation John R. Evans Leaders Fund and the Ontario Research Small Infrastructure Fund to D. S. (43604). The co-authors would like to thank Dr Alexander Wahba at the McGill University Centre for Mass Spectrometry, Montreal, QC, for mass spectrometry analysis of RNA samples. The co-authors are also grateful to Dr Jianqun Wang from the Carleton Nano Imaging Facility for assistance with TEM and EDX analyses of siRNA nanostructures. The co-authors would like to gratefully acknowledge Dr Henrique Piva and the Tissue Engineering and Applied Materials Core Facility (RRID:SCR_022968) for their support and assistance with confocal laser scanning microscopy, fluorescence microscopy and Raman microspectroscopy. The co-authors would also like to thank Mitchell Allen for assistance with statistical analysis and CD spectroscopy, gratefully accessed in the DeRosa lab, as well as Luca Menard for sample preparation for flow cytometry and confocal microscopy.

References

1 P. Guo, The emerging field of RNA nanotechnology, *Nat. Nanotechnol.*, 2010, **5**, 833–842.
2 G. C. Shukla, F. Haque, Y. Tor, L. M. Wilhelmsson, J. J. Toulmé, H. Isambert, P. Guo, J. J. Rossi, S. A. Tenenbaum and B. A. Shapiro, A boost for the emerging field of RNA nanotechnology, *ACS Nano*, 2011, **5**, 3405–3418.
3 P. Guo, F. Haque, B. Hallahan, R. Reif and H. Li, Uniqueness, advantages, challenges, solutions, and perspectives in therapeutics applying RNA nanotechnology, *Nucleic Acid Ther.*, 2012, **22**, 226–245.
4 K. A. Afonin, B. Lindsay and B. A. Shapiro, Engineered RNA Nanodesigns for Applications in RNA Nanotechnology, *DNA RNA Nanotechnol.*, 2015, **1**, 1–15.
5 D. Jasinski, F. Haque, D. W. Binzel and P. Guo, Advancement of the Emerging Field of RNA Nanotechnology, *ACS Nano*, 2017, **11**, 1142–1164.
6 D. W. Binzel, X. Li, N. Burns, E. Khan, W. J. Lee, L. C. Chen, S. Ellipilli, W. Miles, Y. S. Ho and P. Guo,

Thermostability, Tunability, and Tenacity of RNA as Rubbery Anionic Polymeric Materials in Nanotechnology and Nanomedicine-Specific Cancer Targeting with Undetectable Toxicity, *Chem. Rev.*, 2021, **121**, 7398–7467.

7 O. I. Wilner, D. Yesodi and Y. Weizmann, RNA Nanostructures: From Structure to Function, *Bioconjugate Chem.*, 2023, **34**, 30–36.

8 T. Yip, X. Qi, H. Yan and Y. Chang, Therapeutic applications of RNA nanostructures, *RSC Adv.*, 2024, **14**, 28807–28821.

9 N. B. Leontis, A. Lescoute and E. Westhof, The Building Blocks and Motifs of RNA Architecture, *Curr. Opin. Struct. Biol.*, 2006, **16**, 279–287.

10 J. M. Stewart, RNA nanotechnology on the horizon: Self-assembly, chemical modifications, and functional application, *Curr. Opin. Chem. Biol.*, 2024, **81**, 102479.

11 L. Jaeger and A. Chworos, The architectonics of programmable RNA and DNA nanostructures, *Curr. Opin. Struct. Biol.*, 2006, **16**, 531–543.

12 C. Geary, A. Chworos, E. Verzemnieks, N. R. Voss and L. Jaeger, Composing RNA Nanostructures from a Syntax of RNA Structural Modules, *Nano Lett.*, 2017, **17**, 7095–7101.

13 S. H. Ko, M. Su, C. Zhang, A. E. Ribbe, W. Jiang and C. Mao, Synergistic self-assembly of RNA and DNA molecules, *Nat. Chem.*, 2010, **2**, 1050–1055.

14 C. Geary, G. Grossi, E. K. S. McRae, P. W. K. Rothemund and E. S. Andersen, RNA origami design tools enable cotranscriptional folding of kilobase-sized nanoscaffolds, *Nat. Chem.*, 2021, **13**, 549–558.

15 W. K. Kasprzak, N. A. Ahmed and B. A. Shapiro, Modeling ligand docking to RNA in the design of RNA-based nanostructures, *Curr. Opin. Biotechnol.*, 2020, **63**, 16–25.

16 A. Wienecke and A. Laederach, A novel algorithm for ranking RNA structure candidates, *Biophys. J.*, 2022, **121**, 7–10.

17 A. Khaled, S. Guo, F. Li and P. Guo, Controllable self-assembly of nanoparticles for specific delivery of multiple therapeutic molecules to cancer cells using RNA nanotechnology, *Nano Lett.*, 2005, **5**, 1797–1808.

18 K. A. Afonin, M. Kireeva, W. W. Grabow, M. Kashlev, L. Jaeger and B. A. Shapiro, Co-transcriptional assembly of chemically modified RNA nanoparticles functionalized with siRNAs, *Nano Lett.*, 2012, **12**, 5192–5195.

19 K. A. Afonin, M. Viard, A. Y. Koyfman, A. N. Martins, W. K. Kasprzak, M. Panigaj, R. Desai, A. Santhanam, W. W. Grabow, L. Jaeger, E. Heldman, J. Reiser, W. Chiu, E. O. Freed and B. A. Shapiro, Multifunctional RNA nanoparticles, *Nano Lett.*, 2014, **14**, 5662–5671.

20 K. A. Afonin, M. Viard, I. Kagiampakis, *et al.*, Triggering of RNA interference with RNA-RNA, RNA-DNA, and DNA-RNA nanoparticles, *ACS Nano*, 2015, **9**, 251–259.

21 F. Pi, D. W. Binzel, T. J. Lee, *et al.*, Nanoparticle orientation to control RNA loading and ligand display on extracellular vesicles for cancer regression, *Nat. Nanotechnol.*, 2018, **13**, 82–89.

22 K. Jin, Y. C. Liao, T. C. Cheng, *et al.*, *In Vitro* and *In Vivo* Evaluation of the Pathology and Safety Aspects of Three- and Four-Way Junction RNA Nanoparticles, *Mol. Pharm.*, 2024, **21**, 718–728.

23 D. Esmaeilpour, M. Ghomi, E. N. Zare and M. Sillanpää, Nanotechnology-Enhanced siRNA Delivery: Revolutionizing Cancer Therapy, *ACS Appl. Bio Mater.*, 2025, **8**, 4549–4579.

24 W. W. Grabow and L. Jaeger, RNA self-assembly and RNA nanotechnology, *Acc. Chem. Res.*, 2014, **47**, 1871–1880.

25 M. Chandler, M. Panigaj, L. A. Rolband and K. A. Afonin, Challenges to optimizing RNA nanostructures for large scale production and controlled therapeutic properties, *Nanomedicine*, 2020, **15**, 1331–1340.

26 D. Hattab, A. M. Gazzali and A. Bakhtiar, Clinical Advances of siRNA-Based Nanotherapeutics for Cancer Treatment, *Pharmaceutics*, 2021, **13**, 1009.

27 A. Maina, B. A. Blackman, C. J. Parronchi, E. Morozko, M. E. Bender, A. D. Blake and D. Sabatino, Solid-phase synthesis, characterization and RNAi activity of branch and hyperbranch siRNAs, *Bioorg. Med. Chem. Lett.*, 2013, **23**, 5270–5274.

28 M. R. Patel, S. D. Kozuch, C. N. Cultrara, R. Yadav, S. Huang, U. Samuni, J. Koren, G. Chiosis and D. Sabatino, RNAi Screening of the Glucose-Regulated Chaperones in Cancer with Self-Assembled siRNA Nanostructures, *Nano Lett.*, 2016, **16**, 6099–6108.

29 S. D. Kozuch, C. N. Cultrara, A. E. Beck, C. J. Heller, S. Shah, M. R. Patel, J. Zilberberg and D. Sabatino, Enhanced Cancer Theranostics with Self-Assembled, Multilabeled siRNAs, *ACS Omega*, 2018, **3**, 12975–12984.

30 S. S. Shah, C. N. Cultrara, S. D. Kozuch, M. R. Patel, J. A. Ramos, U. Samuni, J. Zilberberg and D. Sabatino, Direct Transfection of Fatty Acid Conjugated siRNAs and Knockdown of the Glucose-Regulated Chaperones in Prostate Cancer Cells, *Bioconjugate Chem.*, 2018, **29**, 3638–3648.

31 S. S. Shah, C. N. Cultrara, J. A. Ramos, U. Samuni, J. Zilberberg and D. Sabatino, Bifunctional Au-templated RNA nanoparticles enable direct cell uptake detection and GRP75 knockdown in prostate cancer, *J. Mater. Chem. B*, 2020, **8**, 2169–2176.

32 C. N. Cultrara, S. Shah, S. D. Kozuch, M. R. Patel and D. Sabatino, Solid phase synthesis and self-assembly of higher-order siRNAs and their bioconjugates, *Chem. Biol. Drug Des.*, 2019, **93**, 999–1010.

33 T. Inoue and B. Tsai, The Grp170 nucleotide exchange factor executes a key role during ERAD of cellular misfolded clients, *Mol. Biol. Cell*, 2016, **27**, 1650–1662.

34 A. S. Lee, The glucose-regulated proteins: stress induction and clinical applications, *Trends Biochem. Sci.*, 2001, **26**, 504–510.

35 A. S. Lee, Glucose-regulated proteins in cancer: molecular mechanisms and therapeutic potential, *Nat. Rev. Cancer*, 2014, **14**, 263–276.

36 T. Mitsui, H. Nakano and K. Yamana, Coumarin–fluorescein pair as a new donor–acceptor set for fluorescence energy transfer study of DNA, *Tetrahedron Lett.*, 2000, **41**, 2605–2608.

37 J. O'Grady, Z. Lyu, M. J. Damha and D. Sabatino, Solid Phase Chemical Synthesis of RNA, in *Biological Macromolecule Engineering Technologies*, Meth. Mol. Bio., Springer Publishing, 2026, pp. 1–16.
38 S. Ellipilli, J. D. Phillips and J. M. Heemstra, Synthesis of comb-shaped DNA using a non-nucleosidic branching phosphoramidite, *Org. Biomol. Chem.*, 2018, **16**, 4659–4664.
39 R. S. Braich and M. J. Damha, Regiospecific solid-phase synthesis of branched oligonucleotides. Effect of vicinal 2′,5′- (or 2′,3′-) and 3′,5′-phosphodiester linkages on the formation of hairpin DNA, *Bioconjugate Chem.*, 1997, **8**, 370–377.
40 A. Katolik, R. Johnsson, E. Montemayor, J. G. Lackey, P. J. Hart and M. J. Damha, Regiospecific solid-phase synthesis of branched oligoribonucleotides that mimic intronic lariat RNA intermediates, *J. Org. Chem.*, 2014, **79**, 963–975.
41 S. Raddatz, J. Mueller-Ibeler, J. Kluge, *et al.*, Hydrazide oligonucleotides: new chemical modification for chip array attachment and conjugation, *Nucleic Acids Res.*, 2002, **30**, 4793–4802.
42 A. N. Chuvilin, M. V. Serebryakova, I. P. Smirnov and G. E. Pozmogova, Byproduct with altered fluorescent properties is formed during standard deprotection step of hexachlorofluorescein labeled oligonucleotides, *Bioconjugate Chem.*, 2009, **20**, 1441–1443.
43 M. Lu, Q. Guo, N. C. Seeman and N. R. Kallenbach, Drug binding by branched DNA: selective interaction of the dye Stains-All with an immobile junction, *Biochemistry*, 1990, **29**, 3407–3412.
44 U. Chheda, S. Pradeepan, E. Esposito, S. Strezsak, O. Fernandez-Delgado and J. Kranz, Factors Affecting Stability of RNA - Temperature, Length, Concentration, pH, and Buffering Species, *J. Pharm. Sci.*, 2024, **113**, 377–385.
45 D. E. Draper, A guide to ions and RNA structure, *RNA*, 2004, **10**, 335–343.
46 T. Miyahara, H. Nakatsuji and H. Sugiyama, Similarities and Differences between RNA and DNA Double-Helical Structures in Circular Dichroism Spectroscopy: A SAC-CI Study, *J. Phys. Chem. A*, 2016, **120**, 9008–9018.
47 K. Sipa, E. Sochacka, J. Kazmierczak-Baranska, M. Maszewska, M. Janicka, G. Nowak and B. Nawrot, Effect of base modifications on structure, thermodynamic stability, and gene silencing activity of short interfering RNA, *RNA*, 2007, **13**, 1301–1316.
48 A. Imhof, M. Megens, J. J. Engelberts, D. T. N. de Lang, R. Sprik and W. L. Vos, Spectroscopy of Fluorescein (FITC) Dyed Colloidal Silica Spheres, *J. Phys. Chem. B*, 1999, **103**, 1408–1415.
49 T. Thomsen, A. B. Ayoub, D. Psaltis and H. A. Klok, Fluorescence-Based and Fluorescent Label-Free Characterization of Polymer Nanoparticle Decorated T Cells, *Biomacromolecules*, 2021, **22**, 190–200.
50 L. Wang, A. K. Gaigalas, J. Blasic, M. J. Holden, D. T. Gallagher and R. Pires, Fluorescence resonance energy transfer between donor-acceptor pair on two oligonucleotides hybridized adjacently to DNA template, *Biopolymers*, 2003, **72**, 401–412.
51 S. K. Motwani, R. K. Khar, F. J. Ahmad and S. Chopra, Effect of solvents quality on determination of particle size and polydispersity of nanoparticles, *J. Exp. Nanosci.*, 2006, **1**, 307–316.
52 S. Bhattacharjee, DLS and zeta potential - What they are and what they are not?, *J. Controlled Release*, 2016, **235**, 337–351.
53 O. Piétrement, V. Arluison and C. Lavelle, RNA Nanostructure Molecular Imaging, *Methods Mol. Biol.*, 2020, **2113**, 319–327.
54 A. J. Lushnikov, Y. I. Avila, K. A. Afonin and A. V. Krasnoslobodtsev, Characterization of RNA Nanoparticles and Their Dynamic Properties Using Atomic Force Microscopy, *Methods Mol. Biol.*, 2023, **2709**, 191–202.
55 F. Xiao, X. Shen, W. Tang and D. Yang, Emerging Trends in DNA Nanotechnology-Enabled Cell Surface Engineering, *JACS Au*, 2025, **5**, 550–570.
56 J. M. Stewart, RNA nanotechnology on the horizon: Self-assembly, chemical modifications, and functional applications, *Curr. Opin. Chem. Biol.*, 2024, **81**, 102479.
57 H. Guo, H. Ding, X. Tang, M. Liang, S. Li, J. Zhang and J. Cao, Quercetin induces pro-apoptotic autophagy via SIRT1/AMPK signaling pathway in human lung cancer cell lines A549 and H1299 in vitro, *Thorac. Cancer*, 2021, **12**, 1415–1422.
58 S. H. Hsu, B. Yu, X. Wang, Y. Lu, C. R. Schmidt, R. J. Lee, L. I. Lee, S. T. Jacob and K. Ghoshal, Cationic lipid nanoparticles for therapeutic delivery of siRNA and miRNA to murine liver tumor, *Nanomedicine*, 2013, **9**, 1169–1180.
59 D. Vocelle, C. Chan and S. P. Walton, Endocytosis Controls siRNA Efficiency: Implications for siRNA Delivery Vehicle Design and Cell-Specific Targeting, *Nucleic Acid Ther.*, 2020, **30**, 22–32.
60 K. S. Lee, Z. Landry, F. C. Pereira, *et al.*, Raman microspectroscopy for microbiology, *Nat. Rev. Methods Primers*, 2021, **1**, 80.
61 A. Z. Samuel, K. Sugiyama, M. Ando and H. Takeyama, Direct imaging of intracellular RNA, DNA, and liquid-liquid phase separated membraneless organelles with Raman microspectroscopy, *Commun. Biol.*, 2022, **5**, 1383.
62 K. J. Kobayashi-Kirschvink, C. S. Comiter, S. Gaddam, T. Joren, E. I. Grody, J. R. Ounadjela, K. Zhang, B. Ge, J. W. Kang, R. J. Xavier, P. T. C. So, T. Biancalani, J. Shu and A. Regev, Prediction of single-cell RNA expression profiles in live cells by Raman microscopy with Raman2RNA, *Nat. Biotechnol.*, 2024, **42**, 1726–1734.
63 J. M. Benevides, M. Tsuboi, J. K. Bamford and G. J. Thomas, Polarized Raman spectroscopy of double-stranded RNA from bacteriophage phi6: local Raman tensors of base and backbone vibrations, *Biophys. J.*, 1997, **72**, 2748–2762.
64 S. Xia, W. Duan, W. Liu, X. Zhang and Q. Wang, GRP78 in lung cancer, *J. Transl. Med.*, 2021, **19**, 118.

65 G. B. Qiao, R. T. Wang, S. N. Wang, S. L. Tao, Q. Y. Tan and H. Jin, GRP75-mediated upregulation of HMGA1 stimulates stage I lung adenocarcinoma progression by activating JNK/c-JUN signaling, *Thorac. Cancer*, 2021, **12**, 1558–1569.
66 X. F. Duan and Y. W. Xin, Overexpression of molecule GRP94 favors tumor progression in lung adenocarcinoma by interaction with regulatory T cells, *Thorac. Cancer*, 2020, **11**, 704–712.
67 H. Wang, A. M. Pezeshki, X. Yu, C. Guo, J. R. Subjeck and X. Y. Wang, The Endoplasmic Reticulum Chaperone GRP170: From Immunobiology to Cancer Therapeutics, *Front. Oncol.*, 2015, **4**, 377.
68 Q. Wang, Z. He, J. Zhang, W. Wang, T. Wang, S. Tong, L. Wang, S. Wang and Y. Chen, Overexpression of endoplasmic reticulum molecular chaperone GRP94 and GRP78 in human lung cancer tissues and its significance, *Cancer Detect. Prev.*, 2005, **29**, 544–551.
69 G. Zhu and A. S. Lee, Role of the unfolded protein response, GRP78 and GRP94 in organ homeostasis, *J. Cell. Physiol.*, 2015, **230**, 1413–1420.
70 T. Suzuki, J. Lu, M. Zahed, K. Kita and N. Suzuki, Reduction of GRP78 expression with siRNA activates unfolded protein response leading to apoptosis in HeLa cells, *Arch. Biochem. Biophys.*, 2007, **468**, 1–14.
71 A. Samih, M. A. de Moura Ferreira and Z. Nikoloski, Gene expression and protein abundance: Just how associated are these molecular traits?, *Biotechnol. Adv.*, 2026, **86**, 108720.
72 R. K. Reddy, C. Mao, P. Baumeister, R. C. Austin, R. J. Kaufman and A. S. Lee, Endoplasmic reticulum chaperone protein GRP78 protects cells from apoptosis induced by topoisomerase inhibitors: role of ATP binding site in suppression of caspase-7 activation, *J. Biol. Chem.*, 2003, **278**, 20915–20924.
73 R. V. Rao, A. Peel, A. Logvinova, G. del Rio, E. Hermel, T. Yokota, P. C. Goldsmith, L. M. Ellerby, H. M. Ellerby and D. E. Bredesen, Coupling endoplasmic reticulum stress to the cell death program: role of the ER chaperone GRP78, *FEBS Lett.*, 2002, **514**, 122–128.
74 J. Petiti, L. Revel and C. Divieto, Standard Operating Procedure to Optimize Resazurin-Based Viability Assays, *Biosensors*, 2024, **14**, 156.
75 G. Hilan, G. Daniel, F. Collak, D. Sabatino and W. G. Willmore, Cancer-Targeting Peptides Functionalized with Polyarginine Enables GRP78-Dependent Cell Uptake and siRNA Delivery Within the DU145 Prostate Cancer Cells, *J. Pept. Sci.*, 2025, **31**, e70007.
76 S. Engelberg, E. Netzer, Y. G. Assaraf, *et al.*, Selective eradication of human non-small cell lung cancer cells using aptamer-decorated nanoparticles harboring a cytotoxic drug cargo, *Cell Death Dis.*, 2019, **10**, 702.
77 I. Waheed, A. Ali, H. Tabassum, N. Khatoon, W. F. Lai and X. Zhou, Lipid-based nanoparticles as drug delivery carriers for cancer therapy, *Front. Oncol.*, 2024, **10**, 1296091.

